Conference Proceedings of the Society for Experimental Mechanics Series

Evro Wee Sit · Chad Walber · Patrick Walter
Alfred Wicks · Steve Seidlitz *Editors*

Sensors and Instrumentation, Aircraft/Aerospace and Energy Harvesting, Volume 8

Proceedings of the 36th IMAC, A Conference and Exposition on Structural Dynamics 2018

SEM

Springer

Conference Proceedings of the Society for Experimental Mechanics Series

Series Editor

Kristin B. Zimmerman, Ph.D.
Society for Experimental Mechanics, Inc.,
Bethel, CT, USA

More information about this series at http://www.springer.com/series/8922

Evro Wee Sit • Chad Walber • Patrick Walter • Alfred Wicks • Steve Seidlitz
Editors

Sensors and Instrumentation, Aircraft/Aerospace and Energy Harvesting, Volume 8

Proceedings of the 36th IMAC, A Conference and Exposition on Structural Dynamics 2018

Springer

Editors
Evro Wee Sit
Svcommunity com
Hermosa Beach, CA, USA

Patrick Walter
Texas Christian University
Fort Worth, TX, USA

Steve Seidlitz
Cummins (United States)
St. Paul, MN, USA

Chad Walber
PCB Piezotronics, Inc
Depew, NY, USA

Alfred Wicks
Virginia Polytechnic Institute & State University
Blacksburg, VA, USA

ISSN 2191-5644 ISSN 2191-5652 (electronic)
Conference Proceedings of the Society for Experimental Mechanics Series
ISBN 978-3-319-74641-8 ISBN 978-3-319-74642-5 (eBook)
https://doi.org/10.1007/978-3-319-74642-5

Library of Congress Control Number: 2018941837

© The Society for Experimental Mechanics, Inc. 2019
This work is subject to copyright. All rights are reserved by the Publisher, whether the whole or part of the material is concerned, specifically the rights of translation, reprinting, reuse of illustrations, recitation, broadcasting, reproduction on microfilms or in any other physical way, and transmission or information storage and retrieval, electronic adaptation, computer software, or by similar or dissimilar methodology now known or hereafter developed.
The use of general descriptive names, registered names, trademarks, service marks, etc. in this publication does not imply, even in the absence of a specific statement, that such names are exempt from the relevant protective laws and regulations and therefore free for general use.
The publisher, the authors and the editors are safe to assume that the advice and information in this book are believed to be true and accurate at the date of publication. Neither the publisher nor the authors or the editors give a warranty, express or implied, with respect to the material contained herein or for any errors or omissions that may have been made. The publisher remains neutral with regard to jurisdictional claims in published maps and institutional affiliations.

Printed on acid-free paper

This Springer imprint is published by the registered company Springer International Publishing AG part of Springer Nature.
The registered company address is: Gewerbestrasse 11, 6330 Cham, Switzerland

Preface

Sensors and Instrumentation, Aircraft/Aerospace and Energy Harvesting represents one of nine volumes of technical papers presented at the 36th IMAC, A Conference and Exposition on Structural Dynamics, organized by the Society for Experimental Mechanics, and held in Orlando, Florida, February 12–15, 2018. The full proceedings also include volumes on Nonlinear Dynamics; Dynamics of Civil Structures; Model Validation and Uncertainty Quantification; Dynamics of Coupled Structures; Special Topics in Structural Dynamics; Structural Health Monitoring, Photogrammetry and DIC; Rotating Machinery, Vibro-Acoustics and Laser Vibrometry; and Topics in Modal Analysis and Testing.

Each collection presents early findings from experimental and computational investigations on an important area within sensors and instrumentation and other structural dynamics areas. Topics represent papers on calibration, smart sensors, practical issues improving energy harvesting measurements, shock calibration and shock environment synthesis, and applications for aircraft/aerospace structures.

The organizers would like to thank the authors, presenters, session organizers, and session chairs for their participation in this track.

Hermosa Beach, CA, USA — Evro Wee Sit
Depew, NY, USA — Chad Walber
Fort Worth, TX, USA — Patrick Walter
Blacksburg, VA, USA — Alfred Wicks
St. Paul, MN, USA — Steve Seidlitz

Contents

Chapter 1
Broadband Energy Harvesting Performance of a Piezoelectrically Generated Bistable Laminate

Andrew J. Lee and Daniel J. Inman

Abstract The vibration based energy harvesting performance of a piezoelectrically generated bistable laminate consisting of only Macro Fiber Composites (MFC) is experimentally characterized. Conventionally, piezoelectric transducers are bonded onto thermally induced bistable composite laminates and exhibit broadband cross-well dynamics that are exploited for improved power generation over linear resonant harvesters. Recently, a novel method of inducing bistability was proposed by bonding two actuated MFCs in a $[0^{MFC}/90^{MFC}]_T$ layup and releasing the voltage post cure to create in-plane residual stresses and yield two cylindrically stable configurations. Forward and backward frequency sweeps at multiple acceleration levels across the first two observed modes of the laminate's two states are performed to identify all dynamic regimes and the corresponding voltages produced by each MFC. Besides single-well oscillations, snap throughs are observed in intermittencies, subharmonic, chaotic, and limit cycle oscillations across wide frequency ranges. Resistor sweeps are conducted for each regime to determine maximum power outputs, and single and multi-frequency performance metrics accounting for laminate volume, mass, input accelerations, and frequencies are evaluated for the laminate. A performance comparison with conventional bistable composite harvesters demonstrate the laminate's viability for energy harvesting, allowing it to be multi-functional in combination with its snap through morphing capability.

1.1 Introduction

Broadband energy harvesting applications enabled by nonlinear adaptive structures under vibration have been and continue attracting significant attention from researchers. This is due to the harvesters retaining efficiency when ambient vibrational energy is distributed over a wide spectrum where the spectral density may be variable over time and dominant at low frequencies [1]. In contrast, linear harvesters are suited only for stationary and narrowband excitation at their fundamental resonant frequencies which limit their usefulness in more realistic environments. To broaden the usable bandwidth during operation, nonlinearities inherent in bistable oscillators have been exploited by numerous past works [2–4] as an efficient and robust mechanism to convert vibrations into electrical energy. These structures have two stable equilibrium states with each corresponding to a distinct geometric configuration, and transition between states occur through buckling, or a nonlinear jump phenomenon known as snap through. Depending on the excitation frequency and amplitude, bistable structures exhibit multiple dynamic regimes that are distinct. This includes single-well vibrations around either of the stable configurations, or cross-well vibrations causing both periodic and aperiodic snap through between both stable equilibria. In certain cases, multiple regimes may coexist under the same vibrational input, but only one is physically realizable depending on the initial conditions. Cross-well regimes such as high amplitude limit cycle oscillations have shown to significantly improve power generation over linear resonance as the harvesters displace between states under high velocities [5]. The attraction to bistable harvesters derive from being able to trigger cross-well vibrations associated with large deformations across a wide range of excitation conditions, which alleviate the performance limitations experienced by their linear counterparts.

Various mechanisms to induce bistability for the purpose of broadband energy harvesting have been explored in past investigations. Popular concepts include obtaining bistability in a cantilevered ferromagnetic beam with magnetic attraction [6, 7], destabilizing a cantilevered beam with a magnetic tip mass from its neutral position with magnetic repulsion [8–10], buckling a clamped-clamped beam with an axial load to obtain a mechanically induced bistable structure [11, 12], and generating internal thermal stresses within a unsymmetric composite laminate during cooldown in its cure cycle which result

---

A. J. Lee (✉) · D. J. Inman
Department of Aerospace Engineering, University of Michigan, Ann Arbor, MI, USA
e-mail: ajle@umich.edu

E. Wee Sit et al. (eds.), *Sensors and Instrumentation, Aircraft/Aerospace and Energy Harvesting, Volume 8*,
Conference Proceedings of the Society for Experimental Mechanics Series, https://doi.org/10.1007/978-3-319-74642-5_1

in two stable configurations [13–22]. As for the energy harvesting method, piezoelectric materials are attached to bistable structures to convert vibration induced strains to electrical energy due to their large power densities, ease of fabrication and application over other methods such as electrostatic, electromagnetic, and magnetostrictive transduction. Recently, a novel means of generating bistability with piezoelectric actuation was investigated by the authors [23, 24]. By bonding two actuated Macro Fiber Composites (MFC) in a cross ply layup and shutting off the power post cure, two stable states are generated through the production of in-plane residual stresses. This is due to the applied electric field causing anisotropic strains within the MFCs from the mismatch of their effective piezoelectric constants. The mechanics are analogous to how a bistable composite laminate is manufactured through the mismatch of its coefficients of thermal expansion between plies [25].

The efficiency gained from simultaneously being the harvester and the primary structure may alleviate challenges inherent in conventional bistable composite harvesters. A design conflict exists where larger piezoelectric patches could generate more energy, but reduces the curvature of the host structure and thus limits its response amplitudes and strains along the patch's polarization direction. In addition, the increased stiffness from larger piezoelectric layers raise the vibrational energy requirement for cross-well dynamics. To mitigate this issue, Betts et al. [26] determined optimal layups, aspect ratios, and piezoelectric areas for a bistable composite harvester. This conflict is avoided by the entirely piezoelectric harvester since it lacks the stiffness of the host composite laminate while retaining the curvatures generated by the MFCs. Its lower stiffness implies that the vibrational energies required for maintaining high energy orbits and broadening cross-well bandwidths are lower than those of conventional bistable composites, and may not require proof masses utilized by many of these harvesters to aid snap through. The proposed harvester however consists of two P1 type MFCs which have a d_{33} poling direction along the piezoceramic fibers with inter-digitated electrodes, and are not ideal for energy harvesting applications due to their low capacitance which limits the current output [27, 28]. In all studies utilizing MFCs as the harvesting unit, the P2 type is chosen which has a d_{31} poling direction through its thickness in a parallel plate configuration, which results in higher capacitance and lower impedance characteristics [15–17, 19, 20]. Despite this, only the P1 type MFCs operate with a high enough piezoelectric coefficient and voltage range necessary for generating bistability [24].

The purpose of this paper is to investigate the energy harvesting performance of the piezoelectrically generated bistable laminate by characterizing its dynamic regimes under harmonic excitation and implementing a simple resistive circuit for energy conversion across the observed modes. Single and multi-frequency metrics available in literature [4, 29] will be utilized to compare the performance of the proposed harvester's regimes and those of bistable composite harvesters due to their similarity in mechanism. These metrics aim to address the issue of establishing fair and appropriate measures of effectiveness for the harvesters by accounting for the excitation input and their physical characteristics. This paper experimentally confirms the laminate's viability for energy harvesting with comparable performance to existing concepts. The authors already demonstrated the bistable laminate's ability to snap through between either stable states with no external assistance by actuating one MFC at a time within its operating limit [24]. The combined morphing and energy harvesting capabilities enable the bistable laminate to be multi-functional with the potential for self-powered morphing and full configuration control.

1.2 Experimental Methodology

1.2.1 Design and Manufacturing

The design of the harvester is catered towards creating the most favorable conditions for inducing bistability and maximizing the range of motion between the stable configurations. The latter condition will enable larger strains to be imparted on the laminate during cross-well vibrations, which will raise the subsequent power output. The simple layup of $[0^{MFC}/90^{MFC}]_T$ is chosen to minimize the total thickness and allow access to the electrodes leads of each MFC, while the cross ply configuration will maximize the out-of-plane displacements of each state [30]. The P1 type MFC utilizing the d_{33} effect is chosen for the voltage actuation required for bistability, and strains in the piezoceramic fiber direction under an operating voltage of −500 to 1500 V. The MFCs are simultaneously actuated at 1500 V while being bonded under vacuum in order to yield the most post cure delta voltage and resulting piezoelectric strains. This also provides the most margin for bifurcation from one to two stable states to occur post cure when the voltage is released. According to previous analysis [23], the critical side length for generating bistability is 85 mm when the aspect ratio of the laminate is 1 and the actuation voltage during bonding is 1500 V. However at this length, the bifurcation voltage is 0 V and this leaves no margin for manufacturing imperfections

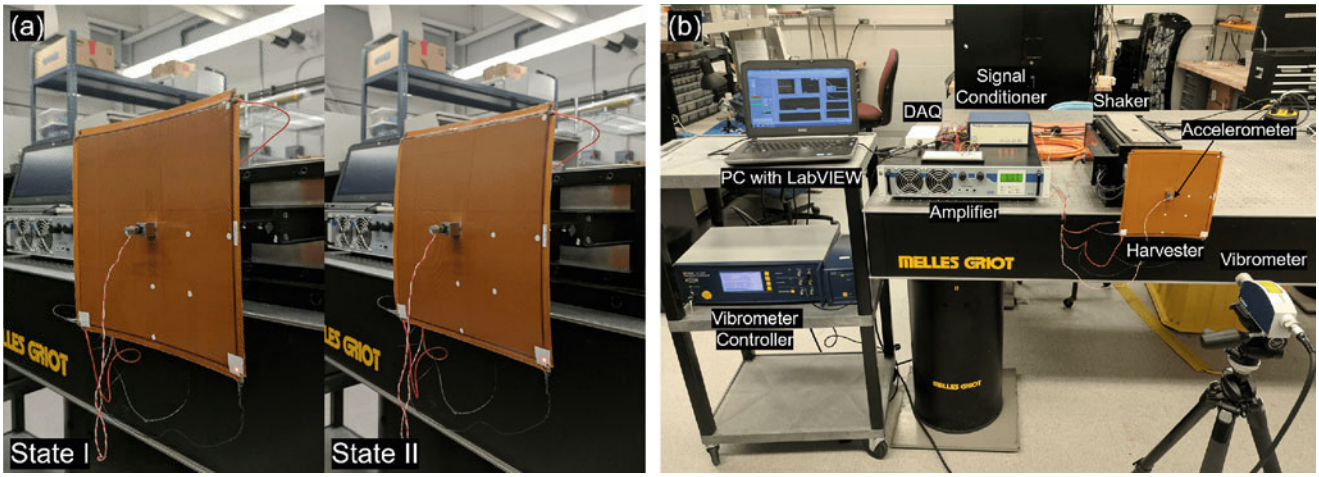

Fig. 1.1 (**a**) Stable states of the $200 \times 200\,\text{mm}^2$ $[0^{MFC}/90^{MFC}]_T$ bistable laminate and (**b**) experimental test setup

while completely limiting the deformation differences between the two resulting configurations. With MFC manufacturing limitations considered, the side length of 200 mm is chosen to ensure sufficiently large displacements and adequate margin for producing bistability.

The $200 \times 200\,\text{mm}^2$ $[0^{MFC}/90^{MFC}]_T$ laminate is manufactured by actuating two P1 type MFCs at 1500 V in parallel with a BK Precision 9130 DC power supply connected to a Trek 2220 high voltage amplifier and bonding them together on a flat tool under vacuum. The MFCs are custom made by Smart Material Corp. and have an active area of $200 \times 200\,\text{mm}^2$, but their total dimensions are $207 \times 218\,\text{mm}^2$ due to the peripheral areas housing the electrode rails and leads between the polyimide films. Therefore, the laminate has 5.5 mm of overhang on each edge with a total bonded area of $207 \times 207\,\text{mm}^2$. The 3M DP-460 epoxy adhesive is used for bonding and cured for 24 h at room temperature. After the cure cycle, the laminate is qualitatively confirmed to be bistable once it is taken out of vacuum and the power to both MFCs are shut off. Figure 1.1a identifies the two stable states of the manufactured $[0^{MFC}/90^{MFC}]_T$ laminate. In this paper, the major curvature axis of state I is along the piezoceramic fiber direction of MFC 1 and that of state II corresponds to MFC 2 in the same manner.

1.2.2 Experimental Setup

Characterizing the $[0^{MFC}/90^{MFC}]_T$ laminate's dynamic regimes and power output under vibrational excitation is achieved with the experimental setup shown in Fig. 1.1b. The harmonic input to the laminate is provided by the APS 113 seismic shaker and powered by the APS 125 amplifier while the laminate is fixed at the center to a stinger that is attached to the shaker. To avoid invasive attachment methods such as drilling a hole and potentially damaging the MFCs, a small neodymium magnet is bonded to the stinger and another identical magnet is then used to mount the laminate onto the stinger. The acceleration at the laminate center is measured by a PCB Piezoelectronics 352C67 accelerometer and the velocity response is measured at a single point by a Polytec OFV-534 laser vibrometer with the Polytec OFV-5000 controller. Reflective tape is adhered to the laminate to improve the signal return of the laser vibrometer. The acceleration, voltage, and velocity responses are recorded with the NI USB-6211 DAQ connected to LabVIEW at a sample rate of 2500 Hz while this combination simultaneously provides the shaker signal based on the acceleration measurements. The voltage responses of each MFC are measured separately and voltage divider circuits are used to reduce the signals to adhere to the DAQ input limit of ±10 V during frequency sweeps. All signals are low-pass filtered and processed in MATLAB. When measuring the harvested power with resistor sweeps, a Tektronix TDS2004C oscilloscope is used to record the root mean square (RMS) voltage output of each MFC without the voltage divider circuits to allow for simple variation of resistive loads, which is quickly implemented with an IET ohmSOURCE resistance box.

1.3 Results and Discussion

1.3.1 Vibration Modes

The dominant modes of the harvester for both stable states are identified with low amplitude forward frequency sweeps and corresponding velocity to base acceleration frequency response functions (FRF) are generated. Determining the resonant frequencies allow subsequent sweep range and locations to be appropriately chosen for characterizing nonlinear dynamic regimes at high excitation amplitudes, since they appear around these modes. Specifically, sweeps are conducted for short and open circuit electrical boundary conditions from 10 to 50 Hz at 0.05 g to minimize nonlinear effects. The velocity measurement locations are at the edges of the active area in the middle of the laminate along the major curvature axis of each state, which allow just their dominant modes to be recorded. Figure 1.2 shows the FRFs of each stable state at low frequencies for the open circuit condition, which are found to be nearly identical to the closed circuit condition.

The first modes of both stable states are identical at 16.58 Hz and exhibit out-of-plane rigid body rotation about the stinger that is inherent to the shaker setup, and is associated with much less elastic deformation than the second mode. The second modes of states I and II are respectively at 27.26 and 26.45 Hz and they are traditional plate bending modes. The slight difference in the second mode indicate that the potential wells of the bistable laminate are not symmetric and reflect the shape discrepancies between the two configurations where state I has higher out-of-plane displacements than state II. This may be due to manufacturing errors involving imperfect layup alignment, a non-uniform epoxy bond line, MFC performance degradation from long actuation times during bonding, and the variation of piezoelectric constants and elastic properties between the two MFCs [24]. These geometric and material imperfections are difficult to control during the manufacturing process, and the resulting state I over state II bias must be considered in the experimental analysis. However, the separation of modes may be advantageous for energy harvesting applications since it extends the total cross-well bandwidth associated with large amplitude oscillations.

1.3.2 High Amplitude Frequency Sweeps

Based on where the linear vibration modes are, forward and backward frequency sweeps at higher amplitudes are conducted in order to identify the nonlinear dynamic regimes of the bistable harvester. The sweeps range from 10 to 34 Hz, which encompass the first two observed modes of each state and the time histories of the base acceleration, corner velocity, MFC

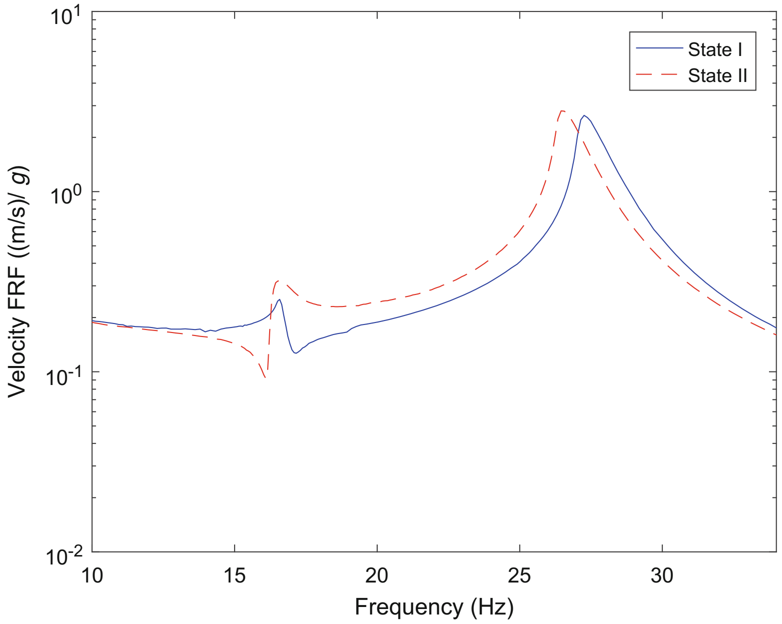

Fig. 1.2 Experimental velocity to base acceleration frequency response function for both stable states

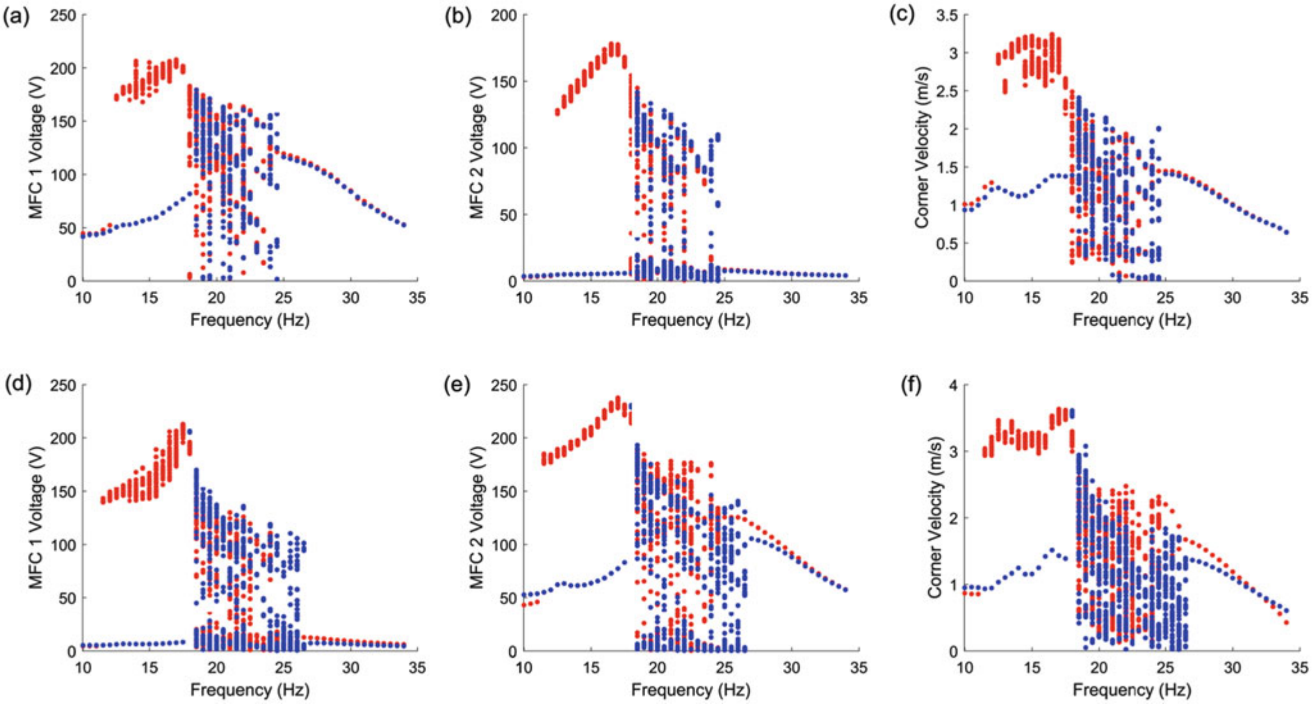

Fig. 1.3 Peak to peak amplitudes in initial state I for (**a**) MFC 1 open circuit voltage, (**b**) MFC 2 open circuit voltage, (**c**) corner velocity, and in initial state II for (**d**) MFC 1 open circuit voltage, (**e**) MFC 2 open circuit voltage, and (**f**) corner velocity during forward (blue) and backward (red) frequency sweeps at 3 g excitation

1 and MFC 2 open circuit voltages are recorded every 0.5 Hz. This procedure is done for input accelerations of 0.5 to 4 g in steps of 0.5 g for both initial states. The corner location is chosen for velocity measurements because it is the only point on the laminate to have significant out-of-plane displacements for both stable configurations, which makes it appropriate for measuring cross-well vibrations from a single location. Peak to peak amplitudes of the recorded time histories are obtained with stroboscopic sampling at excitation frequencies over multiple forcing periods and the resulting figure for 3 g input is shown in Fig. 1.3. This figure is a combination of an FRF and a bifurcation diagram with the excitation frequency being the bifurcation parameter under constant acceleration amplitude [13]. For linear regimes, the sampled amplitude for a given excitation frequency appears as a single point while nonlinear responses are given by multiple points indicating the variation of amplitudes over several consecutive periods. The 3 g acceleration is the lowest excitation level where all dynamic regimes are present for both states, and therefore a suitable input parameter for harvester response and performance characterization.

Note that Fig. 1.3 does not include all coexisting solutions per sweep, but does show some of them due to the nonlinearities inherent to the harvester structure and their dependency on initial conditions. These arise from the softening stiffness effect causing the reduction of resonant frequencies, sweep direction dependent hysteresis forcing the boundaries between single and cross-well regimes to shift, and the asymmetry of the bistable laminate's potential wells causing static state dependent responses and bandwidths [31]. As expected, the strength of these nonlinear effects increase with higher excitation levels. For both states, the softening effect pushes the boundaries between the single and cross-well regions below their second linear modal frequencies regardless of the sweep direction. Hysteretic regions separating the jumps in amplitude are seen from 12.5 to 18 Hz for state I and 11.5 to 17.5 Hz for state II where the backward sweeps induce high amplitude limit cycle oscillations while the forward sweeps remain linear over the same bandwidths, albeit subharmonic resonance can be seen at half the resonant frequency for the bending mode. In contrast, the forward sweeps extend the cross-well regions from 24 to 24.5 Hz for state I and 24.5 to 26.5 Hz for state II over the opposite path. These differences are a consequence of different solutions gaining and losing stability at various frequencies, and are not necessarily the only steady-state solutions in existence. The transition into limit cycle oscillations during backward sweeps may be due to the coalescence of vibrational energy carried by the cross-well motion and the first rigid body mode at 16.58 Hz. Once the backwards sweep passes through the first mode, there is a drop off in amplitude for limit cycle oscillations until returning back to the linear regime. It does not exist in the forward sweep due to the harvester being in low energy orbit when approaching the first mode.

When comparing initial conditions, state II produces a larger 15 Hz cross-well bandwidth over the 12 Hz bandwidth of state I with 2.5 Hz more range for limit cycle oscillations desirable for energy harvesting. In addition, the corner velocities and corresponding output voltages of both MFCs are overall higher for state II. This is due to the out-of-plane displacements being lower for state II, and thus the vibrational energy required to snap through the harvester is also lower. There is a clear correlation between the corner velocity and voltages of the harvester, with cross-well vibrations producing larger amplitudes than their single-well counterparts. During single-well vibrations for state I, MFC 1's voltage output is much higher than MFC 2 due to the induced strains on the former being dominant in the piezoceramic fiber direction associated with the P1 type MFC's primary d_{33} piezoelectric effect, while the latter is prominently strained in the electrode direction normal to the fibers. These dominant strain directions and the ratio of voltage outputs are flipped between MFCs for state II. Once the harvester exhibits cross-well oscillations, the voltage differences are considerably reduced since both MFCs are now operating in the d_{33} mode.

1.3.3 Characterization of Dynamic Responses

Aside from limit cycle oscillations, other nonlinear regimes are associated with lower response amplitudes and include intermittencies, chaotic, and subharmonic oscillations. In Fig. 1.3 over a broad range of amplitudes, several points for a given frequency indicate the presence of harmonics while a dense cluster of points suggest chaotic behavior. However, it provides limited detail and identification of dynamic regime per frequency is difficult, especially for intermittencies consisting of both periodic and aperiodic characteristics. Therefore, the time histories over multiple forcing periods and their corresponding Fourier spectra, phase portraits, and Poincaré maps of every observed regime are analyzed for distinguishing characteristics. This section evaluates example cases for each type of response found in the 3 g frequency sweeps. Figure 1.4 presents the aforementioned plots for high amplitude limit cycle oscillation with input parameters of 14.5 Hz and 3 g during the state I backward sweep. The corner displacements in Fig. 1.4f and subsequent figures are estimated by integrating the corner velocity signal, applying high pass filters to prevent drift, and aligning their peaks with the static corner displacement of state I, which is measured to be 10.42 mm out of plane. The frequency content is obtained with fast Fourier transform (FFT) of time histories recorded during the sweep.

Cross-well limit cycle oscillations are characterized by continuous snap through events which allow a periodic high-energy orbit be sustained between the two stable states. It is associated with the largest velocity and voltage amplitudes out of all dynamic regimes due to the periodic attractor motion having the most penetration into both potential wells, as seen in Fig. 1.4f. The slight asymmetry between states still exist due to the state I initial condition and the state I over II bias

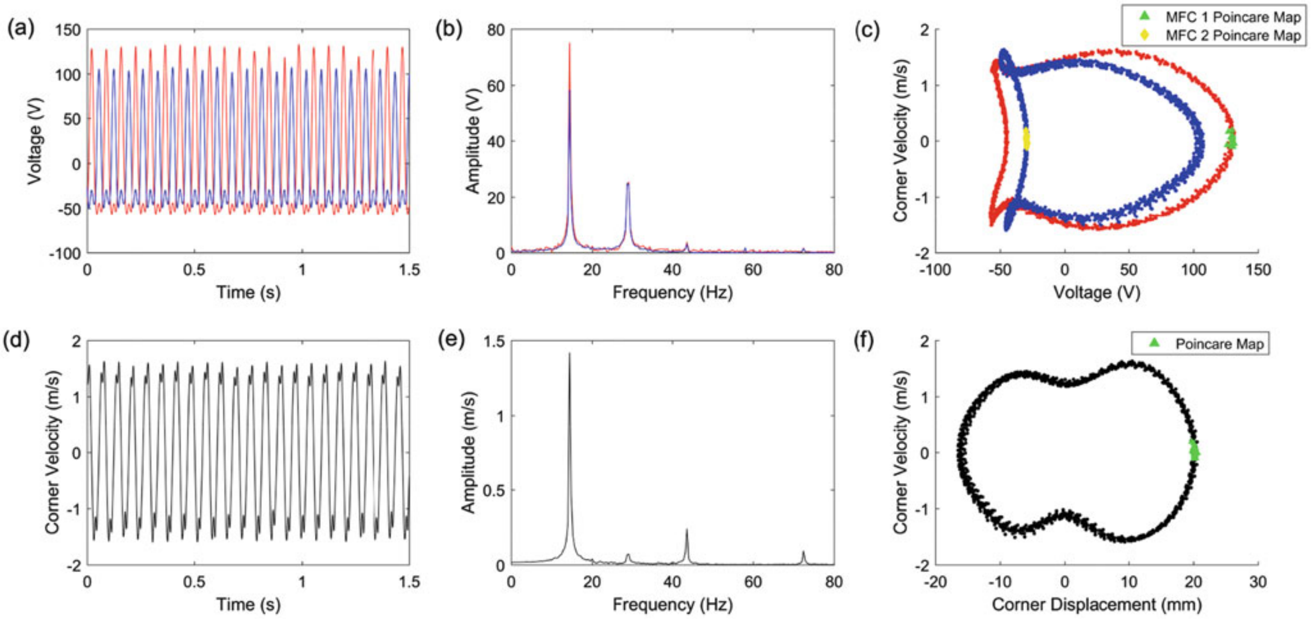

Fig. 1.4 MFC 1 (red) and 2 (blue) open circuit voltages in the forms of (**a**) time histories, (**b**) FFTs, (**c**) phase portraits and Poincaré maps, and corner velocity in the form of (**d**) time history, (**e**) FFT, (**f**) phase portrait and Poincaré map for high amplitude limit cycle oscillations at 14.5 Hz and 3 g during state I backward sweep

discussed previously, but this difference decreases with increasing excitation levels. The electromechanical phase portrait in Fig. 1.4c is enabled by the 90° phase difference between the open circuit voltages and corner velocity. It differs from Fig. 1.4f, where the voltage output is sharply cut when the MFCs are not operating in the d_{33} mode. This effect alternates between MFCs according to their 180° phase difference as also seen in Fig. 1.4a, and is a result of the continuous snap throughs. Consequences of asymmetry and bias towards the initial state are higher output voltages for MFC 1 over 2, and this is correlated by the slightly larger corner velocities and displacements while the harvester is in state I. The Poincaré maps in Fig. 1.4c, f indicate a single-periodic response and the Fourier spectra in Fig. 1.4b, e reveals the associated main harmonic (i.e. ω) of 14.5 Hz to be dominant with 2ω and 3ω superharmonic components contributing much less energy. In contrast to the periodic nature of limit cycle oscillations, Fig. 1.5 presents cross-well chaos under various representations at 18.5 Hz and 3 g in initial state I. To generate enough data for the phase portraits, the measurements are taken separately for 15 min instead of processing the sweep data.

Under chaotic response, the harvester exhibits a strange attractor sensitive to initial conditions [32] as shown in the Poincaré maps in Fig. 1.5c, f, i. The time histories in Fig. 1.5a, d, g reveal that the harvester motion involving snap through events never quite repeats itself, though there are passages of nearly recurrent behavior, and therefore remains completely aperiodic. The FFTs in Fig. 1.5b, e, and h shows a much more broadband spectrum with the primary component being the excitation frequency of 18.5 Hz, but energy is present over a wide range of frequencies. Although the phase portrait trajectories escape the potential well of state I and displays cross-well behavior, the majority of vibration is centered around state I with much less penetration into state II when compared to limit cycle oscillations. Besides limit cycle oscillations, all other cross-well regimes display this same behavior to varying degrees and is attenuated as the acceleration input rises. This growth in asymmetry in combination with infrequent snap through events, lower velocities, and output voltages suggest the chaotic response to be less favorable for harvesting power than the high energy orbits of Fig. 1.4. Figure 1.6 presents the rest of the harvester's dynamic responses in the initial state I 3 g backward sweeps and include subharmonic and linear oscillations at 22.5 and 34 Hz, intermittency between limit cycle and chaotic oscillations at 18 Hz, and intermittency between subharmonic and chaotic oscillations at 20.5 Hz.

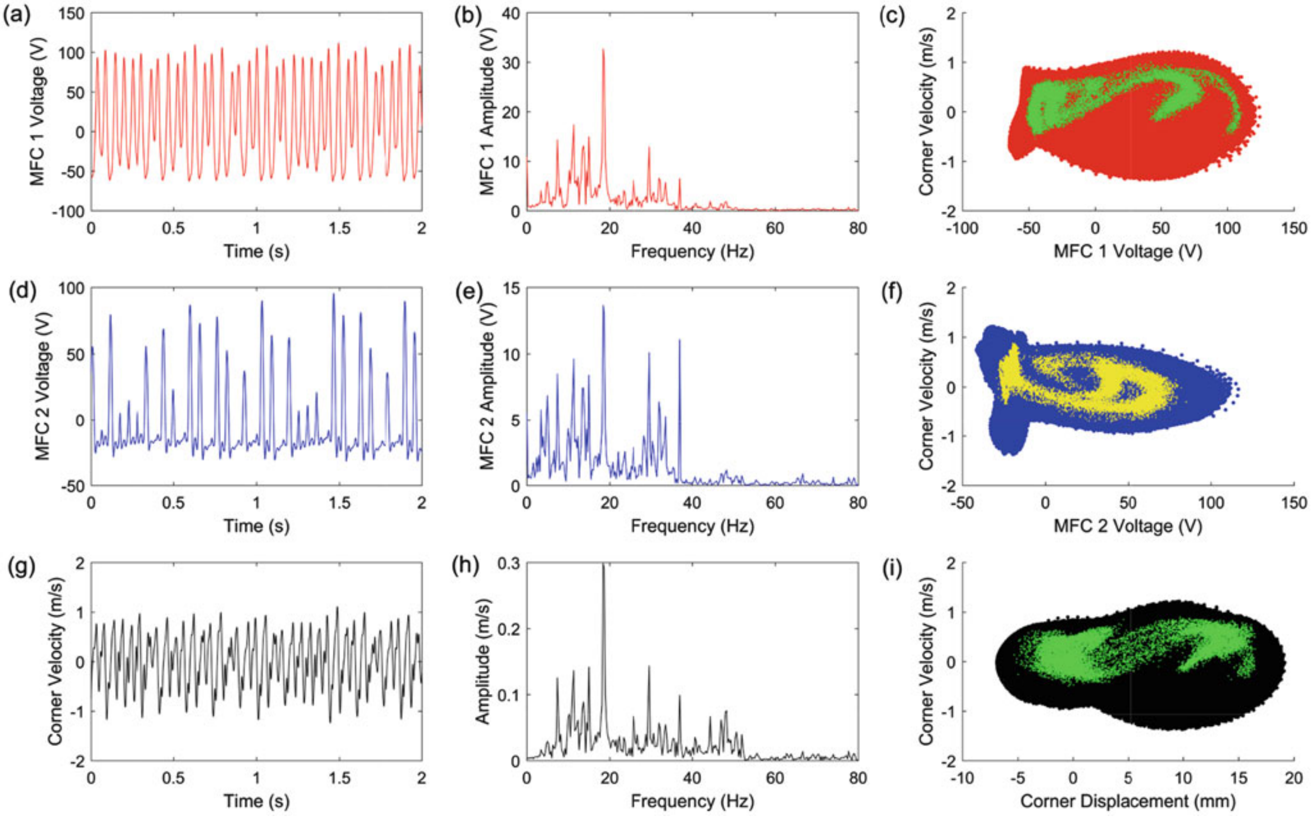

Fig. 1.5 MFC 1 (red) open circuit voltage in the form of (**a**) time history, (**b**) FFT, (**c**) phase portrait and Poincaré map, MFC 2 (blue) open circuit voltage in the form of (**d**) time history, (**e**) FFT, (**f**) phase portrait and Poincaré map, and corner velocity in the form of (**g**) time history, (**h**) FFT, (**i**) phase portrait and Poincaré map for chaotic oscillations at 18.5 Hz and 3 g in initial state I

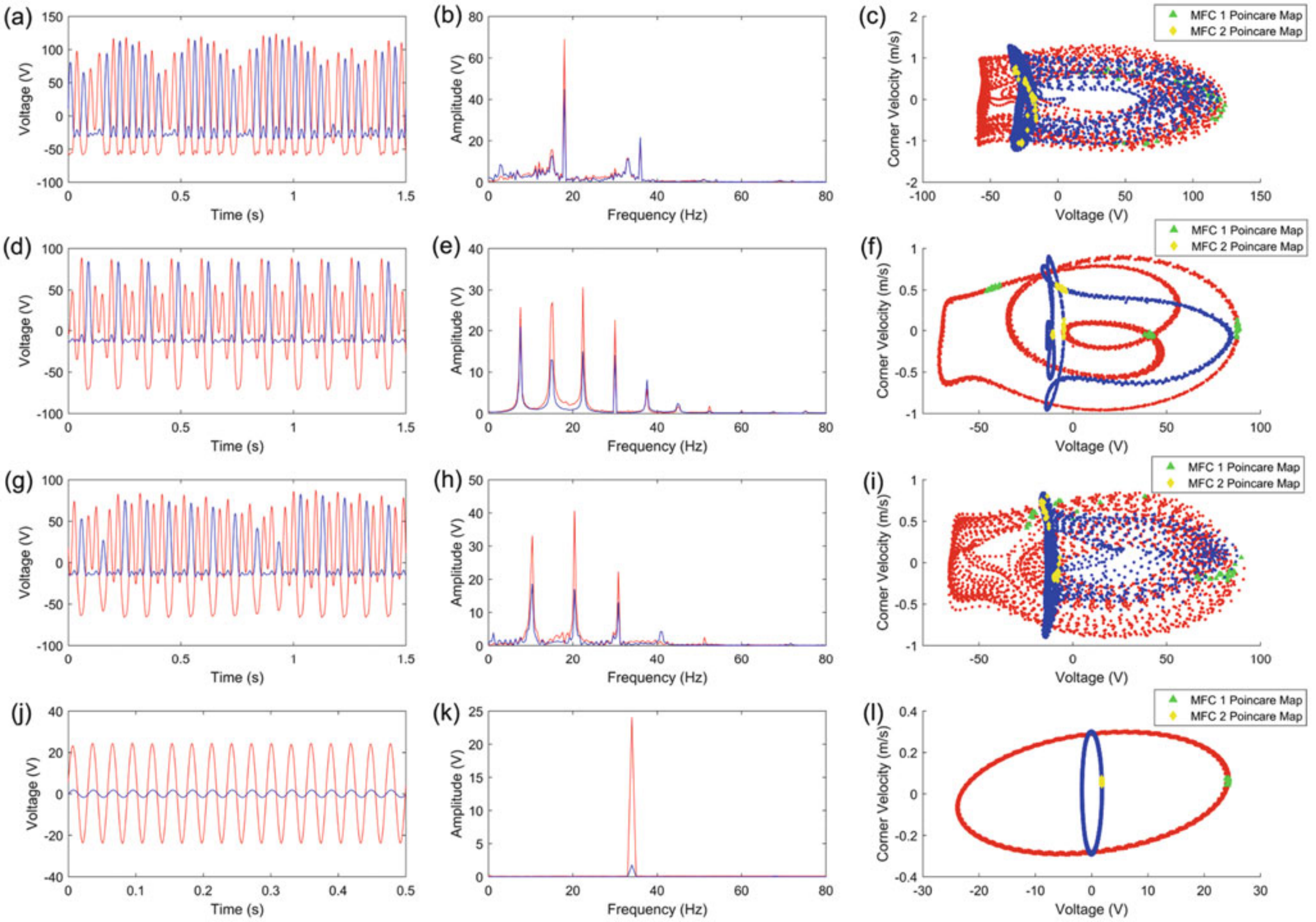

Fig. 1.6 Intermittency between limit cycle and chaos at 18 Hz for MFC 1 (red) and 2 (blue) open circuit voltages in the forms of (**a**) time histories, (**b**) FFTs, (**c**) phase portraits and Poincaré maps, subharmonic oscillations at 22.5 Hz for MFC 1 (red) and 2 (blue) in the forms of (**d**) time histories, (**e**) FFTs, (**f**) phase portraits and Poincaré maps, intermittency between subharmonic and chaotic oscillations at 20.5 Hz for MFC 1 (red) and 2 (blue) in the forms of (**g**) time histories, (**h**) FFTs, (**i**) phase portraits and Poincaré maps, and linear oscillations at 34 Hz for MFC 1 (red) and 2 (blue) in the forms of (**j**) time histories, (**k**) FFTs, (**l**) phase portraits and Poincaré maps during 3 g state I backward sweep

Intermittency is attributed by the sporadic switching between two qualitatively different behaviors while the excitation input is kept constant [33], and these behaviors are cross-well chaos and limit cycle oscillations in the case of Fig. 1.6a–c. The voltage time histories in Fig. 1.6a display the nearly periodic motion interrupted by occasionally irregular bursts that are statistically distributed, causing the respective spread and loss of periodicity in the phase portraits and Poincaré maps in Fig. 1.6c. The FFTs in Fig. 1.6b show that the main excitation frequency and its superharmonic components are still dominant like in Fig. 1.4b, e, but the presence of chaos spreads the energy contribution across the spectrum. The behavior of this regime suggest that its energy harvesting capability is between those of limit cycle and chaotic oscillations. Figure 1.6d–f exhibits cross-well subharmonic oscillations, or specifically a period-3 oscillation that takes 3 forcing periods to complete a full cycle [34]. The Poincaré maps in Fig. 1.6f assess the periodicity of the response by sampling it once per period, and reveal three distinct locations within the phase portrait of each MFC. Its frequency content in Fig. 1.6e shows the presence of order-1/3 harmonic components ($\omega/3$, $2\omega/3$, $3\omega/3$, etc) with fairly even distribution, and responsible for inducing the period-3 response. It should be noted that a range of subharmonic oscillations (period-2 through 8) is observed during the frequency sweeps across all excitation levels in both single and cross-well motion, but they are not presented here. Intermittency is also found between subharmonic and chaotic regimes as seen in Fig. 1.6g–i. At 20.5 Hz specifically, irregular alternation of period-2 and chaotic oscillations can be seen in the corresponding time histories and the Poincaré maps reveal the spreading of two distinct clusters for both MFCs, indicating the aperiodic nature within the subharmonic response. FFTs show the dominance of order-1/2 harmonic components ($\omega/2$, $2\omega/2$, $3\omega/2$, etc) with contributions by in-between frequencies resulting from the intermittent chaos. The harvester's final dynamic regime is single-well linear oscillations as seen in Fig. 1.6j–l at the non-resonant frequency of 34 Hz. As expected, the two MFC voltage signals are periodic and in phase with each other, MFC 1 outputs much larger values, and the only frequency component is the excitation signal.

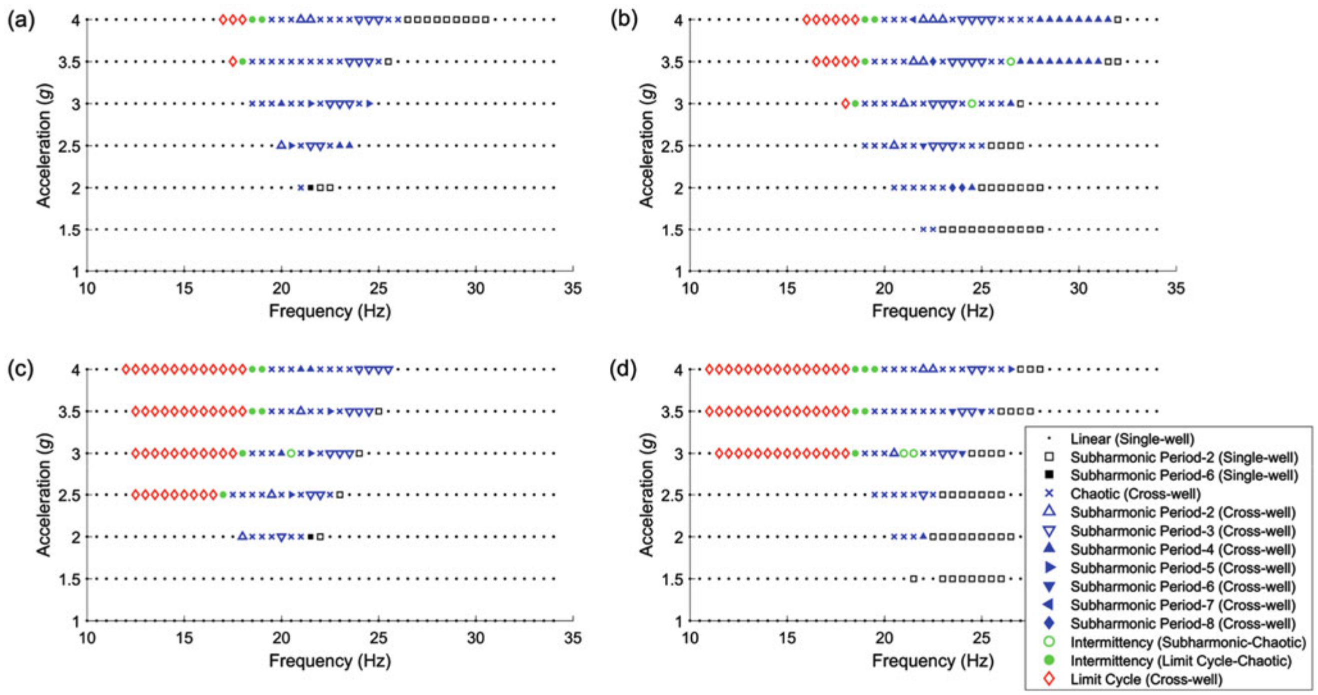

Fig. 1.7 Observed dynamic responses at multiple acceleration levels during forward frequency sweeps with initial (**a**) state I, (**b**) state II, and during backward frequency sweeps with initial (**c**) state I, and (**d**) state II

With all of the observable dynamic regimes characterized, the rest of the frequency sweep data at other acceleration inputs are evaluated to identify how the harvester responds under a range of excitation levels. A summary of this evaluation is shown in Fig. 1.7, but note that not all coexisting solutions are present. At 0.5 g, nonlinear effects such as softening and hysteresis discussed previously are minimal and resonance is seen very close to the plate bending mode at 27.26 and 26.45 Hz for states I and II. With higher accelerations, the strength of nonlinearities rise where the bending mode frequency is pushed backwards, hysteretic regions and subharmonic resonance grow, and single-well subharmonic oscillations are observed near the resonant frequency. Cross-well vibration in the form of chaos first appears at 1.5 g forward sweep for state II at the reduced resonant frequency of 22 Hz, and the rest of the sweeps follow suit with the addition of cross-well subharmonic oscillations at 2 g. As the excitation level continues to increase, the cross-well bandwidth is extended primarily in the direction that the sweep is in. High amplitude limit cycle oscillations first appear during the 2.5 g backward sweep for state I at 16.5 Hz and its bandwidth grows with higher acceleration levels at the expense of other cross-well regimes. As expected, intermittencies are observed between the regimes they are respectively alternating from. At 4 g, the total cross-well bandwidth is 14 Hz for state I and 20.5 Hz for state II due to the asymmetry of potential wells.

1.3.4 Energy Harvesting Capability

Excluding limit cycle oscillations, Fig. 1.3 shows that the open circuit voltage amplitudes of cross-well regimes are similarly ranged, and this holds true for other acceleration levels. Even after accounting for the steady rise in maximum amplitudes towards the onset of limit cycle oscillations, it is not clear how each regime's average power output will compare relative to each other due to their intermixing in this bandwidth, and warrants further investigation. To evaluate the energy harvesting capability of the harvester, resistor sweeps are conducted across 1, 1.78, 3.16, 5.62, 10, 15.8, 25.1, 39.8, 63.1, 100, 178, 316, 562 kΩ, and 1 MΩ in order to match the impedance of each MFC to the load resistance, which maximizes their power output. With each MFC, the sweeps are run at 3 g for the observed regimes outlined in the previous section, and the results are presented in Figs. 1.8 and 1.9 for states I and II. The excitation frequencies are where the maximum power is generated for each regime with the exception of cross-well subharmonic oscillations, which are chosen to be period-3 for both states to allow fair comparison. As observed in [7], the range of load resistances in the sweeps do not suppress any of the nonlinear phenomena (i.e. shunt damping effect) exhibited by the harvester, and so it is able to maintain the cross-well responses